Biosensors and Bioelectronics 255 (2024) 116198

Contents lists available at ScienceDirect

Biosensors and Bioelectronics

journal homepage: www.elsevier.com/locate/bios

# Nonwoven fiber meshes for oxygen sensing

Nikolaos Salaris [a,b], Wenqing Chen [a,b], Paul Haigh [c], Lorenzo Caciolli [b,d], Giovanni Giuseppe Giobbe [d], Paolo De Coppi [d,e], Ioannis Papakonstantinou [f], Manish K. Tiwari [a,b,*]

[a] Nanoengineered Systems Laboratory, UCL Mechanical Engineering, University College London, London, WC1E 7JE, United Kingdom
[b] Wellcome/EPSRC Centre for Interventional and Surgical Sciences-WEISS, University College London, London, W1W 7TS, United Kingdom
[c] School of Engineering, Newcastle University, Newcastle, NE1 7RU, United Kingdom
[d] NIHR Biomedical Research Centre, Stem Cells and Regenerative Medicine, Developmental Biology and Cancer Programme, UCL GOS ICH Zayed Centre for Research Into Rare Disease in Children, 20 Guilford Street, London, WC1N 1DZ, United Kingdom
[e] Dept. of Specialist Neonatal and Paediatric Surgery, Great Ormond Street Hospital, London, UK
[f] Photonic Innovations Lab, Department of Electronic and Electrical Engineering, University College London, London, WC1E 7JE, United Kingdom

ARTICLE INFO

*Keywords:*
Optical oxygen sensing
Solution blowing
Polymer fibers
Fiber/silicone rubber composites

ABSTRACT

Accurate oxygen sensing and cost-effective fabrication are crucial for the adoption of wearable devices inside and outside the clinical setting. Here we introduce a simple strategy to create nonwoven polymeric fibrous mats for a notable contribution towards addressing this need. Although morphological manipulation of polymers for cell culture proliferation is commonplace, especially in the field of regenerative medicine, non-woven structures have not been used for oxygen sensing. We used an airbrush spraying, i.e. solution blowing, to obtain nonwoven fiber meshes embedded with a phosphorescent dye. The fibers serve as a polymer host for the phosphorescent dye and are shown to be non-cytotoxic. Different composite fibrous meshes were prepared and favorable mechanical and oxygen-sensing properties were demonstrated. A Young's modulus of 9.8 MPa was achieved and the maximum oxygen sensitivity improved by a factor of ~2.9 compared to simple drop cast film. The fibers were also coated with silicone rubbers to produce mechanically robust sensing films. This reduced the sensing performance but improved flexibility and mechanical properties. Lastly, we are able to capture oxygen concentration maps via colorimetry using a smartphone camera, which should offer unique advantages in wider usage. Overall, the introduced composite fiber meshes show a potential to significantly improve cell cultures and healthcare monitoring via absolute oxygen sensing.

## 1. Introduction

Oxygen sensing via phosphorescence quenching has emerged as a solution in a multitude of healthcare areas ranging from cancer research (Shi et al., 2014) (Stone et al., 1993) to cell culture monitoring (Papkovsky and Dmitriev, 2013) (Grist et al., 2010). Fluorescence guided surgery has taken advantage of obtaining real time data on tissue vascularization (Paraboschi et al., 2021). However, information on vascular network does not always reliably correlate to the local oxygen support, which is ultimately the relevant information needed. The choice of matrix material for the encapsulation of the phosphorescent dyes is important, especially for monitoring the oxygen concentration in biological environments. To this end, the main characteristics of interest for the host materials are: permeability to oxygen; mechanical and chemical stability; solubility in solvents used to dissolve the dye; biocompatibility and optically favorable properties.

Among many choices, a common approach is the use of silicone-based rubbers to encapsulate the dye molecules. Polydimethylsiloxane (PDMS) is the most common example (Amao, 2003) (Xue et al., 2014). However, a number of disadvantages emerge when using PDMS in tissue engineering, for both oxygen monitoring and its use as a scaffold. The hydrophobic nature of PDMS hampers its effectiveness for bio-engineered tissue growth (Ratner et al., 2004), and its tendency to induce dye aggregation during curing results in an inhomogeneous dye distribution (Li et al., 2021). Additionally, when used in microfluidic chambers, the absorption of biological molecules onto their surfaces and the high permeability of PDMS to water vapor led to the chamber drying (Favre et al., 1994).

* Corresponding author. Room 503E, Roberts Building, Torrington Place, London, WC1E 7JE, United Kingdom.
*E-mail address:* m.tiwari@ucl.ac.uk (M.K. Tiwari).

https://doi.org/10.1016/j.bios.2024.116198
Received 12 October 2023; Received in revised form 5 March 2024; Accepted 7 March 2024
Available online 27 March 2024

As an alternative, a widely accepted polymer that over time became the predominant material for cell culture growth is polystyrene. Its cost-effective fabrication, ability to modify its surface structure with straightforward techniques, and biochemical inertness render are desirable properties (Lerman et al., 2018). In addition, a great deal of the literature focuses on surface treatment of the materials used in bioreactors to enhance cell adhesion, proliferation and differentiation (Lee et al., 2013). For example, apart from the appropriate scaffolding material, vital growth factors and chemical differentiators, numerous studies in tissue engineering and regenerative medicine have focused on the manipulation of mechanical and structural characteristics of the cell's microenvironment. The goal of these techniques is to produce the appropriate stimuli that mimic *in vivo* conditions and lead to cell proliferation and differentiation (Wang et al., 2001), (Gerecht et al., 2007), (Altman et al., 2002), (Garvin et al., 2003). Some common and inexpensive methodologies that have been proposed in the literature, such as the breath figure (BF) technique, have focused on inducing porosity on the substrate surface of the petri dishes (Huang et al., 2014), (Bui et al., 2018), (Gerecht-Nir et al., 2004). The study of porous materials for oxygen sensitive dye encapsulation has also been presented with phase inversion techniques (Lee and Park, 2017). Nonetheless, the brittle nature of the polymers obtained do not allow for macroscale bioengineered tissue development. This has been described as crucial in regenerative medicine studies elsewhere, such as for a patient transplanted with tissue engineered trachea (Ahn et al., 2019) and cancer research (Wu et al., 2018).

Fiber meshes are a promising alternative (Caicedo-Carvajal et al., 2011), (Sun et al., 2005). For the fabrication of fibrous materials from polymers, electrospinning has shown promising results (Leong et al., 2016), (Baker et al., 2006), (Kumar and Vasita, 2017). A crucial advantage of this fabrication technique is the ability to vary the size and porosity of the fibrous meshes, which results in the capacity to mimic the tissue microstructure depending on the cell culture application (da Silva et al., 2010); a fact especially important in extracellular matrices for load-bearing tissue such as cartilage, tendons and ligaments (Vunjak-Novakovic et al., 2004), (Agarwal et al., 2008), (Jun et al., 2018). However, drawbacks include the prerequisites of high voltages and electrically conductive targets, and a low deposition rate. Another technique to produce nano- and micro-fibers is solution blowing of polymer fibers (Dadol et al., 2020). This method offers scalability and low-cost fabrication (Tutak et al., 2013) by relying on dissolving the polymers with solvents and blowing the solution onto a target using a high velocity gas to drive the process. This allows for significantly faster production times at a fraction of the cost (Zhang et al., 2009). Additionally, it provides the ability to tune fiber thickness and induce porosity on its surface (Polat et al., 2016), (Gao et al., 2021), and has been shown to achieve rapid conformal deposition on any type of surface, including biological material (Behrens et al., 2014a).

Moreover, wearable electronics with favorable mechanical characteristics that allow them to conform to the human body has been the focus of many studies, both in and out of the clinical setting (Biswas et al., 2020). Commercial wearables are still composed of rigid materials which renders their use obtrusive and in need of additional supports (such as belts or bendable strips). In fact, numerous clinical devices that are in use today limit the monitoring of physiological parameters in the laboratory rather than providing on-patient remote health monitoring (Lim et al., 2020). Fundamentally, this poses a bottleneck for their adoption, which could help reduce the ever-increasing cost of healthcare (Majumder et al., 2017). Therefore, it is imperative to replace existing materials with skin-like alternatives for enhanced wearability and functionality. Flexible sensors based on silicone rubbers and fibrous polymer films pose as a possible solution to address these difficulties by providing the user comfort and compliant mechanics (Guo et al., 2016).

Furthermore, there is a pressing clinical need for a sensing methodology that can provide real time, non-invasive and cost-effective oxygen concentration measurements for would healing monitoring (Sen, 2009). Tissue oxygenation (oxygen dissolved in biological fluids of tissue) plays a pivotal role in the duration and effectiveness of the wound healing process (Bishop, 2013). Specifically, cell proliferation, collagen synthesis, response to infections, angiogenesis and cell migration rely on oxygen availability. From a materials point of view, many types of biomaterials have been tested in terms of their biocompatibility and flexibility, as well as their oxygen sensing properties (Tavakol et al., 2020), (Mostafalu et al., 2015), (Ochoa et al., 2020). Both electrochemical (Ochoa et al., 2020) and optical means (Mostafalu et al., 2015) of oxygen detection have been applied. Additionally, spatially resolved oxygen mapping of inflamed tissue has been shown using near infrared spectroscopy (Webb et al., 2015) and phosphorescence-based (Li et al., 2014) sensing technologies. Despite these promising results, clinical practices have largely not incorporated such sensing methodologies.

Numerous studies have successfully achieved polymer encapsulation of phosphorescent dyes; however, despite the advantages noted above, the fabrication of flexible, biocompatible and mechanically robust sensing films from fiber meshes has not been reported up to date. Here, we propose the embedding of the phosphorescent dye PtOEP in a nonwoven fiber mesh by solution blowing a solvent based polymer solution using Tetrahydrofuran (THF) and Dimethylformamide (DMF). The selection of the dye was based on its high quantum efficiency and is commonly used for oxygen sensing via quenching of phosphorescence. Both porous and nonporous fibers were fabricated, and different blends of polymers were tested by combining polystyrene (PS) with: i) a commercial silicone rubber (Ecoflex 00–50), ii) thermoplastic polyurethane (TPU) and iii) ethyl cellulose (EC). The characterization of their chemical composition, morphology and mechanical properties was performed using FTIR, scanning electron microscopy (SEM) and mechanics load-deformation measurements. The resulting fiber meshes yielded excellent oxygen sensing properties: high sensitivity, low response time and lack of cytotoxicity. Mechanically robust encapsulation of the fibers was also demonstrated, albeit with reduction in sensing properties, and the variation of relative humidity was shown to hamper their performance. 2D Oxygen concentration maps were also captured via colorimetry using a smartphone camera.

## 2. Materials and methods

### 2.1. Materials, fabrication and instrumentation

For the fabrication of the polymer fiber meshes a spraying approach (solution blowing) was used. Specifically, an airbrush (Iwata LPH-80 LVLP) with a 1.0 mm nozzle was employed along with an air pump (05295 SIP 6 compressor) and a nitrogen gas tank. The main polymer of choice was polystyrene (MW ~ 230,000, Merck), the oxygen sensitive, phosphorescent dye used was PtOEP (Platinum Octaethylporphyrin, 95%, Merck), purchased as nanopowder, and the solvents used to dissolve the polymer were chloroform ($CHCl_3$), tetrahydrofuran (THF) ($\leq$ 99.9 %, Merck) and dimethylformamide (DMF) (n,n-dimethylformamide, anhydrous, ($\leq$ 99.8 %, Merck). The polymers used for the composite fibers were a silicone rubber, i.e. Ecoflex 00–50 (Smooth-On Inc.), Ethyl cellulose (48.0–49.5 wt % ethoxyl basis, Merck) and Ravathane thermoplastic polyurethane (TPU) pellets (Ravago).

Fourier transform infrared spectroscopy (FTIR) (iS50 FT-IR, NicoLet) was performed to determine the composition of the fiber meshes and scanning electron microscopy (SEM) (Zeiss EVO 25) was used to obtain magnified images and measure the distribution of their fiber diameters and pore sizes. The mechanical properties of the fiber meshes were determined using a mechanical testing system (Discovery DMA850) and samples cut with the standard dimensions of ASTM D412 Type 4 (Fig. S1.1, Supplementary Material). Also, cyclic tests to assess the flexibility of the samples were performed using a linear actuator (AZSSMUK). Additional coating of the fibers was performed using Ecoflex, polydimethylsiloxane (PDMS) (Sylgard 184) and polyvinyl acetate (PVA) (MW 85,000–124,000, 99+% hydrolyzed, Merck). For the coated

films, tensile tests were performed with an Instron mechanical analyser (model 5969, 500 N load cell).

First, we used the solvents THF and DMF to dissolve the phophorescent dye PtOEP by stirring and sonicating in room temperature for 2 h. Then, the resulting solution was mixed with the polymers while keeping the ratio of dye to polymer constant at 0.1 wt %. The first set of fibers involved solution blowing with a single polymer, polystyrene, and the two solvents in different ratios (F1 and F2 type of fiber meshes) (Table S2.1, Supplementary Material). For composite fiber meshes, three separate polymer combinations were tested; PS was mixed with EC, Ecoflex and TPU, i.e. fiber types F3, F4 and F5, respectively (for mixing ratios/chemical compositions see section S2, Supplementary Material).

All fibers were produced using the fabrication technique of solution blowing. Here, this involved employing a commercial air gun, a polymer solution and a high velocity flow of air to create and deposit polymer fibers onto the targeted collection surface (Tutak et al., 2013), (Behrens et al., 2014a), (Srinivasan et al., 2011), (Sinha-Ray et al., 2011) (Fig. 1). In detail, two fluid streams are combined in the spray gun, where one is pressurised air and the other is a polymer solution consisting of the polymer and the solvent (Fig. 1b). Furthermore, the fiber meshes were coated with the silicone derivative rubbers Ecoflex and PDMS by dip coating and were cured in room temperature for Ecoflex and 120 °C, using an oven for 2 h, for PDMS. Additional information on the fabrication method (Solution Blowing) and the setup used in this study is provided in section S3 of the Supplementary Material.

For the characterization of the oxygen sensing properties and their sensitivity to relative humidity levels, simple optoelectronic instrumentation in a reflection-based configuration was employed (this has been described in detail in previous work (Salaris et al., 2022)). This included the use of a photodiode (which included a built-in amplification circuit and a voltage read out) as a light detector (DET100A2, Thorlabs), an LED as a light source (Wurth Elektronic, WL-SUMW Series, 395 nm, 1100 mW) and a power generator (E3631A, Keysight) to power the LED. The calibration tests were performed in an enclosure with the use of oxygen and nitrogen gases (BOC) in a steady flow, which was controlled using mass flow controllers (El-Flow prestige Bronkhorst). The physical mechanism of oxygen sensing in this study is based on the quenching of phosphorescence emitted by the dye (PtOEP) molecules (Papkovsky and Dmitriev, 2013).

### 2.2. Characterization methods

FTIR measurements were employed to determine the composition of the meshes. Both the polymers used to prepare the solutions and the resulting fibers were tested to determine the composition of the latter by comparing the two. For the morphology characterization, images obtained via SEM were used to visualize the resulting surface morphology of the fibers. The same images were also used to measure the range and distribution of fiber diameters, and pore sizes, using the software ImageJ.

The mechanical properties of the fiber meshes, both coated and uncoated, were evaluated using tensile strength and cyclic fatigue tests. For these measurements, the fiber meshes were tested by cutting them into specific molds (Fig. S1.2 and Table S1, Supplementary Material). Additionally, Ecoflex and polystyrene samples (in the form of a dense film) were tested for comparison reasons.

For the characterization of the oxygen sensing properties, the sensitivity, dynamic range, half-sensitivity point, and response time were measured (S4, Supplementary Material). For this, we first calculated the recovery time from 0 % to 20 % oxygen concentration (V/V) and then tested the fiber meshes were sequentially for 7 levels of constant oxygen concentration using the mass flow controllers; 0, 5, 10, 20, 40, 60 and 80 % (V/V) of oxygen. This allowed us to build the Stern – Volmer plots (see section 3.4). The temperature and the total flow of both gases were kept constant (room temperature and 10 l/min, respectively). To calculate the half sensitivity point, the Stern - Volmer plots were fitted with the two-site model (Eq. (1)) (Carraway et al., 1991) using a least squares fitting with the SciPy Python library at a resolution of 1 % V/V. Also, only the Stern - Volmer curve before saturation was fitted to achieve a low error ($R^2$).

$$\frac{I_0}{I} = \left( \sum_{j=1} \frac{f_j}{1 + K_{SV}{}^j [O_2]} \right)^{-1} \quad (1)$$

where $f_j$ is the fraction of each site j and their sum is equal to 1 (for two site model $j = 1,2$), $K_{SV}$ is the Stern-Volmer constant and $[O_2]$ the oxygen concentration. The influence of humidity on the oxygen sensing measurements was also investigated.

For the cytotoxicity tests, a LIVE/DEAD cell viability assay kit (Thermofisher, L3224) was used to evaluate the cell viability for the fiber mesh of type F1.3 on human dermal fibroblast (HDF) cell line.

## 3. Results and discussion

### 3.1. Composition characterization

FTIR was employed to determine the characteristic molecular structure of the fibers by comparing them with the polymers used to produce the solutions. Specifically, this is achieved by identifying the absorption peaks at specific frequencies for the unprocessed polymers

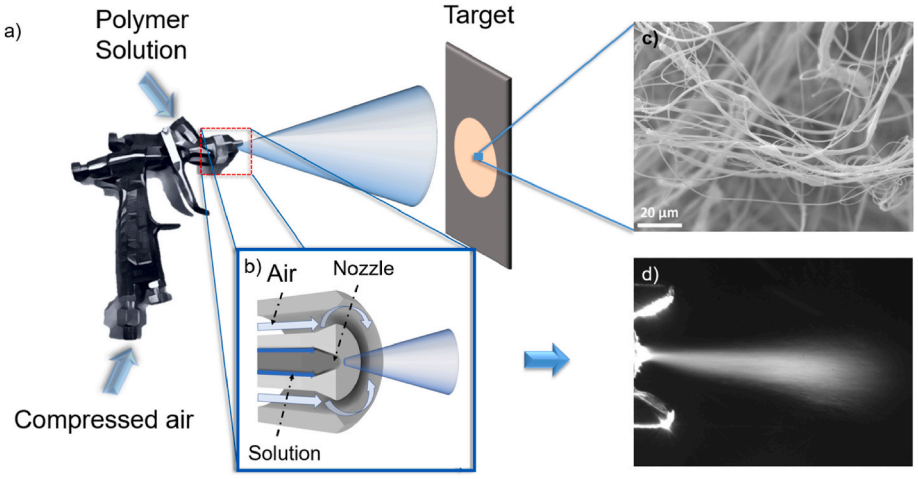


**Fig. 1.** a) Schematic depiction of solution blowing using a spray gun b) Schematic depiction of the nozzle of the spray gun during fabrication, with the direction of the air and solution flow indicated c) SEM image of the resulting fibers and d) image of the spray gun tip during the fiber fabrication.

and then comparing them with the equivalent peaks observed for the fibers. It should be noted that the peaks were compared in terms of their position on the frequency axis and the absorption values were normalized (Fig. 2).

The first set of results showed that the choice of solvent did not affect the chemical composition of the fibers, as both types of fibers F1 and F2 exhibited the same characteristic absorption peak positions (at 2266, 724 and 611 $cm^{-1}$) and similar relative absorption amplitudes (Fig. 2a).

Moreover, for the composite fibers F3, F4 and F5, both the characteristic peaks for polystyrene and the equivalent polymer mixed (e.g. PS and Ecoflex for F4 type of fibers) were present in the absorption spectra to a large degree unchanged (Fig. 2b, c, d). In detail, the spectra of the composite fibers were the additive result of the two polymers mixed in the solution, i.e., the position of the peaks and the relative absorption spectra of the composites were a combination of both the raw materials that they were comprised. This indicated that the resulting fibers were a mixture of the two polymers, which retained largely their chemical composition intact. Additionally, for fiber types F3 and F5, the peak positions were also similar when comparing between the fibers and the raw materials in the solutions. A detailed analysis of the peak positions and their corresponding significance is given in section S5, Supplementary Material.

### 3.2. Morphology characterization

SEM was used to investigate the resulting morphology of the fiber meshes and calculate the fiber diameters and pore areas. Examples of SEM images used for fiber diameter size calculations are shown in Fig. 3a and c, and the results in terms of distribution of fiber diameters for film F3.1 are depicted in Fig. 3b. For the pore size calculations, an example of film F1.3 is shown in Fig. 3d and results are displayed in terms of distribution of pore sizes in Fig. 3e. We observed that the average fiber diameter and the distribution of the fiber diameters were similar for each type of fibers with the same composition. Thus, we concluded that the fiber diameter is related to the polymers in the solutions (Table S6, Supplementary Material).

In detail, fiber meshes of type F5 (PS/TPU) yielded the largest fibers sizes (up to an average of 11.6 ± 4.18 μm) while F4 and F3 the smallest (average of ~1.5 μm). Additionally, the standard deviation over the mean average (coefficient of variation) was calculated for each film and it was shown that all samples yielded high coefficient of variations (Table S6). The relatively high coefficient of variation is attributed to the fabrication technique used (solution blowing), which has been shown to lead to higher variations of fiber diameters (Polat et al., 2016). Notably, fiber type F5 had the lowest variation of fiber diameter and at the same time the largest average fiber diameter. Possibly, smaller fiber diameters seen in fiber types F3 and F4 merged in the other samples (which was

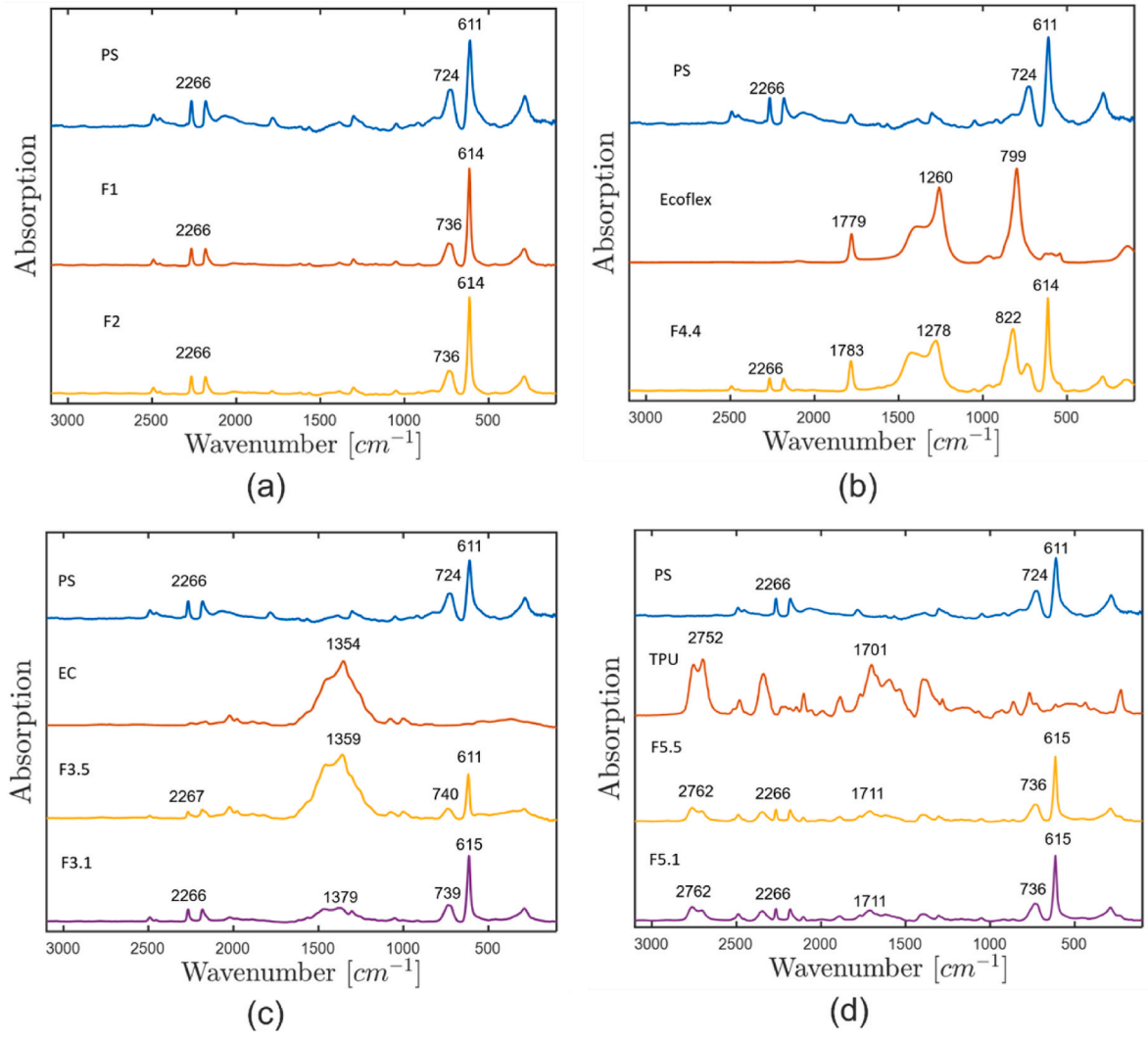


**Fig. 2.** FTIR absorption spectra for: (a) PS and films F1 and F2, (b) PS, Ecoflex and film F4.4, (c) PS, EC and films F3.5 and F3.1, (d) PS. TPU and films F.5.5 and F5.1; with the main peak positions highlighted.

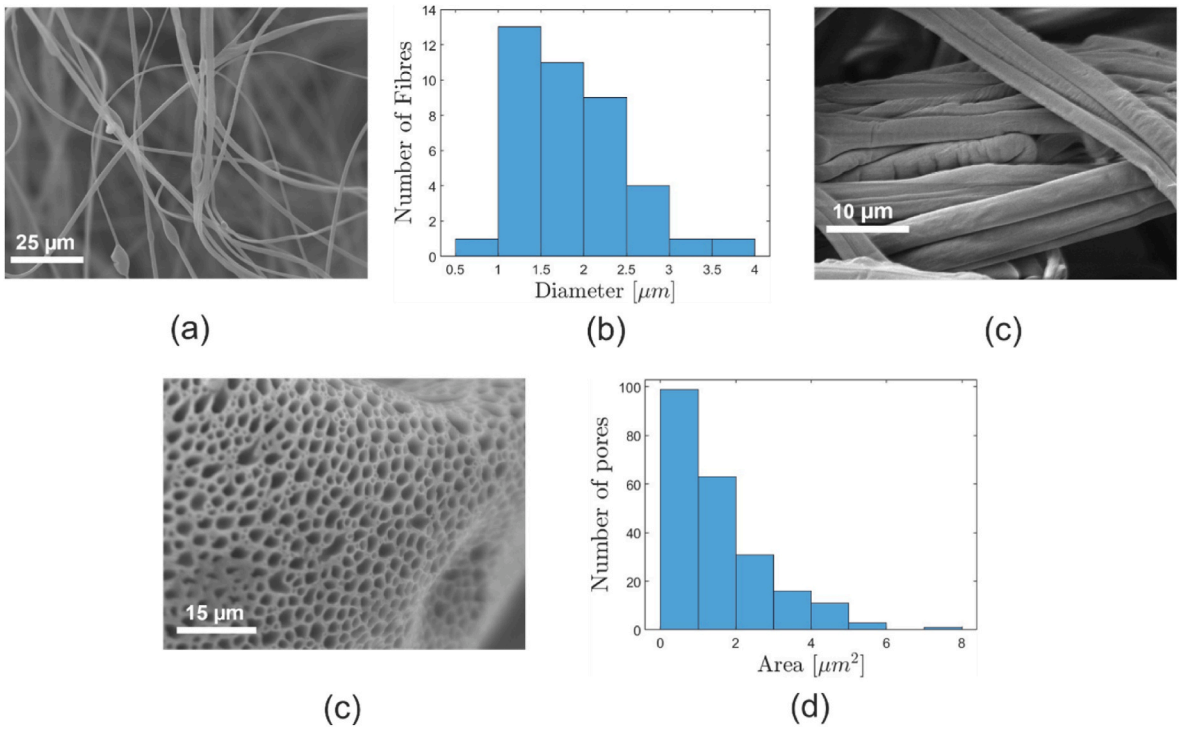


**Fig. 3.** a) SEM image of F3.1, b) Distribution of fiber diameters of F3.1, c) SEM image of F1.3 showing the merging of the fibers d) SEM image of F1.3 showing the porosity of the beads in the fiber mesh and e) the pore area distribution as calculated from ImageJ.

also observable from the SEM images (Fig. 3c) explaining the larger range of fiber diameters. This was also seen when using solution blowing spinning, where the rotor that was used as a target for the fibers, resulting in a smaller average fiber diameter (also described by Zhang et al. (2020)) and a larger coefficient of variation.

Furthermore, F1 and F2 types of fiber yielded similar average diameters regardless of the solvent and polymer concentration in the solutions. However, the increase in the amount of polystyrene in fibers F3 and F4 resulted in larger fiber diameters while the opposite was true for F5. In previous studies the increase in solution concentration resulted in larger fiber diameters (Daristotle et al., 2016), and thus additional studies are required to explain the results shown here for F1, F2 and F5 types of fiber.

Another clear feature were the ball shaped beads (with a size of up to several fiber diameters) that were present throughout the mesh and randomly distributed for all fibers. This was once more attributed to the fabrication method and has been reported before (Sabbatier et al., 2014). Also, the beads in the fiber meshes exhibited porosity when using the air pump. The distribution of the pore surface area was calculated from an SEM image (Fig. 3d) and is presented here for film F1.3 as an example (Fig. 3e). This effect was more prominent in the higher average diameter fiber meshes. Previous studies have suggested that beads are formed in high concentration polymer solutions (Behrens et al., 2014b). Notably, when a dry gas was used (nitrogen from a gas cylinder) no porosity was observed (Fig. S6.1, Supplementary Material), which was attributed to low humidity. The analysis of the pore sizes showed a distribution with a coefficient of variation of ~0.9 and an average pore area of 1.46 $\mu m^2$. It should be mentioned that there was no correlation established between porous and non-porous fiber meshes in terms of oxygen sensing properties. Thus, an in-depth characterization of the porosity of the was not performed and is not relevant to this work.

### 3.3. Mechanical properties

The mechanical properties of the fiber meshes were first evaluated by performing tensile strength measurements. The resulting graphs were analyzed in terms of Young's modulus, maximum tensile stress and maximum strain (Table S7, Supplementary Material). It was observed that depending on fiber composition, different stress versus strain relations were present. Specifically, three different types of deformations were identified across all samples: i) an initial linear increase of stress in relation to strain, ii) a non-linear increase and iii) plateaus of constant stress for increasing strain (Fig. S7, Supplementary Material).

Moreover, for reference purposes, films of pure Ecoflex and PS were also tested; PS yielded a significantly higher modulus and maximum stress and the silicone rubber Ecoflex, yielded a higher maximum strain. This was expected due to the large density and brittleness of PS and the elastic nature of rubbers. In terms of the fiber meshes, different moduli and ultimate strength points (i.e. points where the stress and strain are at maximum) were observed depending on their composition.

In detail, fibers based on polystyrene only (type F1 and F2) presented similar characteristics, with the exception of film F1.3 that produced a higher maximum strain (Fig. S7a). This was attributed to experimental error. Also, when comparing F1.3 to FP1.3, we notice that the use of pressure does not alter the mechanical properties significantly. On the other hand, the use of solution blowing spinning and Ecoflex in the solution (fiber type F4) produced fibers that yielded a lower maximum strain and an increased Young's modulus (Fig. S7b). Film type F3 (PS/EC) produced the highest strains (a maximum of 18 %) but the lowest maximum stress (23 kPa) and modulus (0.24 MPa). However, this was a result of the existence of regions of deformation where the stress was constant while the strain was increasing rapidly (Figs. S7c and S7d). Thus, it was concluded that type F3 fiber meshes were more fragile when compared to the rest.

F4 and F1 type of fibers exhibited similar results. However, it was observed that their mechanical properties depended on the direction of the tensile strength tests in relation to the drum rotation. In other words, there was a directionality of the improved properties based on the alignment of the fibers when collected with the rotating drum. For example, fiber mesh F4.1AC was produced when the mold was cut perpendicular to the direction of the rotation of the drum collector and F4.1AL, when the fibers where cut along the fiber direction. Notably,

F4.1AL had the highest maximum stress (556 kPa) and Young's modulus (9.8 MPa) when compared to the rest of the fibers but showed significantly less maximum strain compared to F4.1AC (4.8% vs 10.7 %, respectively). Additional studies are required to investigate this effect.

Additionally, increasing the ratio of Ecoflex in the solution did not result in further improvement of the properties. This was possibly the result of a reduced alignment above a certain ratio of PS/Ecoflex in the solution due to the lowering of the fiber diameter, but additional studies are required to investigate this. The higher modulus of F5.2 could be explained by the high modulus of TPU when in dense form (Tayfun et al., 2017) although the maximum stress remained low. In the literature, tensile tests for PCL fibers have shown a lower Young's modulus (~2 MPa compared to 9.8 MPa) when using solution blowing but higher maximum stress and strain points when employing electrospinning (up to 35 MPa) (Tutak et al., 2013), (Prabhakaran et al., 2008), (Hong and Kim, 2010), (Nam et al., 2011).

### 3.4. Oxygen sensing properties

The measurements for the characterization of the oxygen sensing properties clearly indicated that the fiber meshes yielded favorable sensing capabilities (Table S8.1, Fig. 4 and Figs. S8.1, S8.2, Supplementary Material). The fiber meshes presented here were compared with their film-like counterpart as a measure of improvement in terms of sensing performance. In detail, the dense film exhibited significantly lower sensitivity and dynamic range compared to the fiber meshes, and simultaneously had a much larger recovery time. Specifically, when comparing the best performing fiber meshes to the dense polystyrene film: a) the maximum sensitivity increased by a factor of ~2.9, b) the recovery time decreased by 96%, c) the half sensitivity point increased 21 % (V/V) and the dynamic range increased by a factor of ~5.6.

When comparing between the different fiber meshes, the highest sensitivity (~11) was achieved with the use of fiber type F4.1 (PS/Ecoflex), which was also accompanied by the largest dynamic range (2.48 V) and half sensitivity point (27 % V/V) (Table S8.1 and Fig. S8.1). In essence, the sensing properties after the addition of Ecoflex in the polymer blend were improved when compared to the fibers composed solely of PS or the use of EC and TPU (Fig. S8.1). In terms of recovery time, all the fibers exhibited similar results with the lowest achieved being 6 s and the highest 20 s. Furthermore, the use of solution blowing spinning showed similar sensing properties when comparing between FS1.3 and F1.3, and the use of DMF as the solvent (F2) yielded less favorable properties.

Moreover, no significant change in the oxygen sensing properties of the fiber meshes was observed when comparing the cases with and without porous beads and no relation between fiber diameter size and oxygen sensing properties was observed. This is clear by comparing Table S6 (average fiber diameter measurements) and Table S8.1 (Supplementary Material) (oxygen sensing properties).

In total, by comparing the fiber meshes described here with phosphorescent films produced with other polymer encapsulation techniques, it is clear that the use of fibers led to a significant increase in sensing performance. In detail, Table 1 compares the improvement in sensing properties of the highest performing fibers presented here with the literature. When compared to previously reported porous films (e.g. produced using the Breath Figure technique), the improvement is less. Nonetheless, contrary to rigid porous structures that are brittle in nature, the fibers shown here offer favorable mechanical properties.

### 3.5. Biocompatibility test

The cell cultures grown from the medium of the control group were compared to the ones grown in the fiber mesh of type F1.3. Details of the cytotoxicity tests are given analytically in section S9, Supplementary Material. The cell cultures corresponding to both the control sample and the fiber mesh are shown in Fig. S9.1. It was observed that the concentration of live cells was ~98 % for the control sample and ~96% (average of three samples) for the fiber mesh in terms of the ratio alive/total cells. The ratio was calculated by counting the nuclei of the live (green stain) and dead cells (red stain). However, the use of calcein lead to the staining of the entire cytoplasmic environment and therefore some experimental error is still present. Nevertheless, these results indicate the low cytotoxicity of the fiber mesh tested (F1.3) and thus its compatibility with cells.

### 3.6. Silicone rubber coating

Additional tests were performed by coating the fiber meshes of type F1.3 and F4.1 with silicone rubbers to produce a mechanically robust and flexible support host for the phosphorescent dyes. The resulting films were tested in terms of their tensile strength properties (Table S10), their fatigue through cyclic testing (section S11) and their

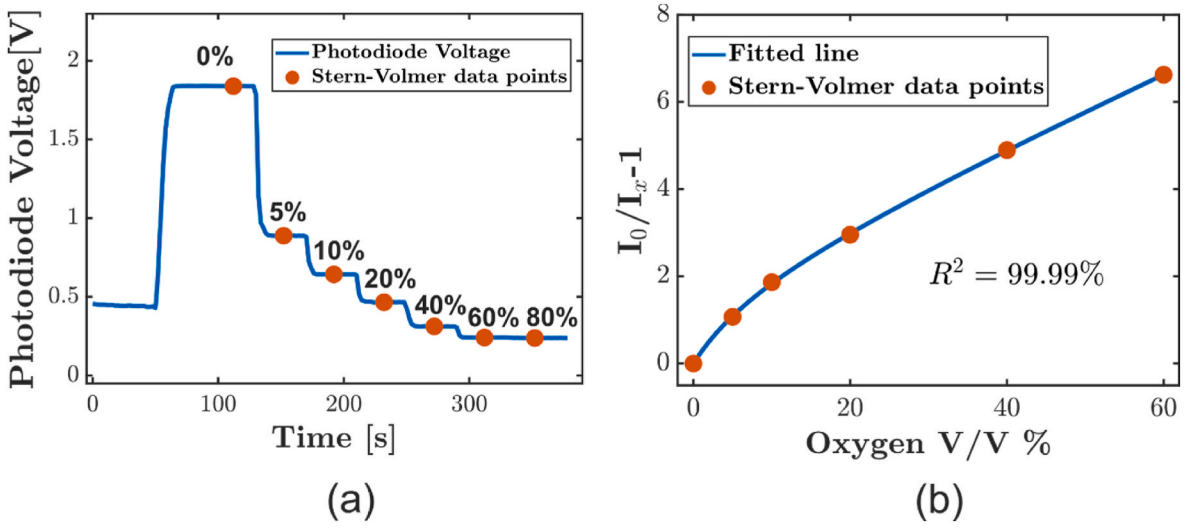


**Fig. 4.** Plots of: a) the output photodiode voltage over the time of sampling during the oxygen sensing tests; each plateau corresponds to a different oxygen concentration (0, 5, 10, 20, 40, 60 and 80% V/V) and the points used for the construction of the Stern-Volmer plot are highlighted; b) the Stern-Volmer plot calculated from the points indicated in (a) and fitted using the two-site model. The fiber mesh of type F5.2 was used here as an example. For all films the curve was fitted up to 60 % V/V due to the saturation of the Stern-Volmer plot after that point for some types of films.

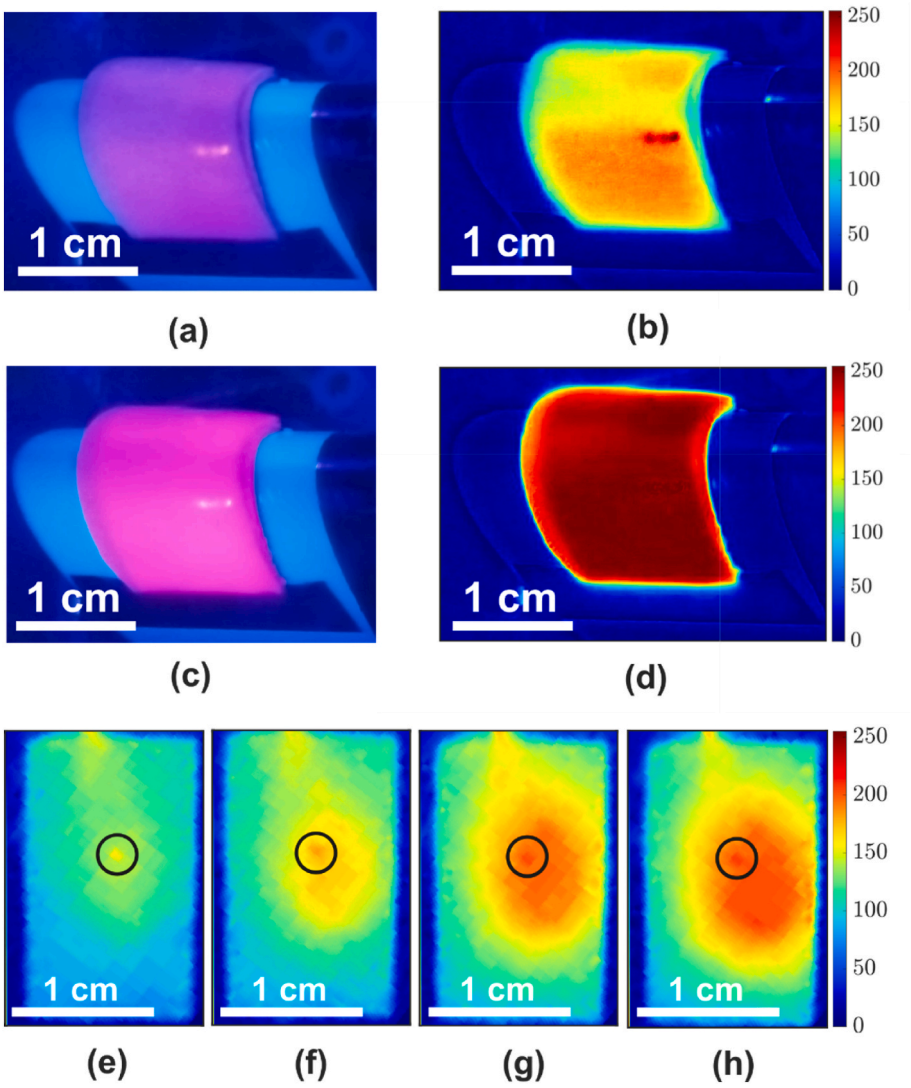


**Fig. 5.** a) Image of the film CF1 for 20% V/V of oxygen b) red channel of image (a) c) image of the film F1.3 for 0 % V/V of oxygen and d) red channel of (c). (e) to (h) depict the red channel of images taken for the different levels of nitrogen flow, 1–4 l/min respectively, through a 3 mm hole with film F1.3. The color bars for (b), (c) and (e) to (h) are depicted using a relative light intensity scale (arbitrary units) from 0 to 255. Scalebars are included for each image and the geometry of the underlying hole for images (e)–(h) has been highlighted.

**Table 1**
Table comparing the improvement in sensing performance via polymer film modification from various studies in the literature and the fiber meshes proposed here. The sensitivity point at 80 % V/V was used in this study as a reference point since above this oxygen concentration the measurements were saturated.

| Polymer | Dye | Metric | Improvement | Fabrication | Ref. |
|---|---|---|---|---|---|
| PS/PEG | – | Luminescent intensity | 60 % | Dropcasting | (Liu et al. (2011)) |
| pSiMC | EuA | Luminescent intensity | 100 % | Etching | (Jenie et al. (2017)) |
| MTEOS | $R(Ph2phen)_3^{2+}$ | $\Delta DR/DR^d$ | 73 % | Dropcasting | (McEvoy et al. (1996)) |
| MTEOS/TEOS | $RuCl_3H_2O$ | $\Delta DR/DR^d$ | 92 % | Dropcasting | (McDonagh et al. (1998)) |
| CAB | PtOEP | $\Delta DR/DR^d$ | 2.8 | Breath Figure | (Salaris et al. (2022)) |
| PS fiber (F4.1) | PtOEP | $\Delta DR/DR^d$ | 4.6 | Solution Blowing | – |
| PS/PEG | PtOEP | $\Delta S_{100}/S_{100}^d$ | 91 % | Dropcasting | (Liu et al. (2013)) |
| PS/PG | PtOEP | $\Delta S_{100}/S_{100}^d$ | 72 % | Phase separation | (Lee and Park (2017)) |
| PDMS-MPA | PtTFPP | $\Delta S_{100}/S_{100}^d$ | 30 | Photo-lithography | (Mao et al. (2017)) |
| CAB | PtOEP | $\Delta S_{100}/S_{100}^d$ | 6.3 | Breath Figure | (Salaris et al. (2022)) |
| PS fiber (F4.1) | PtOEP | $\Delta S_{100}/S_{100}^d$ | 1.9 | Solution Blowing | – |
| PCL | PtTFPP and PdTFPP | – | – | Electrospinning | (Presley et al. (2019)) |
| PS | Eu (TTA)3 (phencarz) | – | – | Electrospinning | (Wang et al. (2011)) |
| MCM-41 | Ru | $\Delta S_{100}/S_{100}^d$ | 2.94 | Electrospinning | (Wang and Yao (2023)) |

sensing performance (Table S12). The stress - strain plots were used once more for the description of the mechanical properties of the samples. In detail, the different sections of the stress strain plots were first identified (Figs. S10.1 and S10.2, Supplementary Material). For reference purposes films of pure Ecoflex, PDMS and PS were tested. Also, the results for the PDMS coated film were presented for comparison reasons since their oxygen sensing properties were not determined due to the large recovery time.

It is clear that the different materials have significantly different moduli and maximum points (section S10, Supplementary Material). In particular, CF1 film yielded the most favorable properties; maximum stress (with the exception of the unprocessed polymers) at 1085 kPa and maximum strain of 9.6. Comparing CF1 to the pure Ecoflex case, the prior exhibits a much higher linearity and a higher Young's modulus. However, at the maximum point, the stress was ~1.6 times larger and the strain was slightly larger (~8%). This was attributed to the fragility of the fibers in the composites that undergo plastic deformation at lower strains. Additional studies should focus on wetting CF1 with varying quantities of Ecoflex and analyze resulting variations in the stress-strain curves.

For the PDMS coated sample (CF3), the composite yielded lower maximum strain characteristics compared to the rest of the coated fibers. This was expected since by comparing Ecoflex and PDMS, it is clear that PDMS is a stronger material (higher maximum stress) but less stretchable (lower maximum strain). It should be noted that when comparing the composites with the pure PDMS case, lower modulus and ultimate stress points were observed. For PVA (CF4), lower ultimate stress points but a high modulus is yielded. However, an important drawback of using PVA is its dependency on the humidity of their environment (Mikulchyk et al., 2013), and thus additional experiments are required to determine its viability in wearable technologies. For dense polystyrene (D1) the maximum stress was much higher but the maximum strain was much smaller (four and three orders of magnitude, respectively). This suggests the tensile strength and brittleness akin to glassy polymers. This further emphasizes the advantage of the fiber meshes and the composites described here for sensor applications that require a high surface area and flexibility.

Furthermore, additional flexibility tests were performed for CF1. A, F1.3 and D1. This involved the use of cyclic fatigue testing for a 1-point bending motion (section S11, Supplementary material). It was observed that the dense PS film fractured at ~170 cycles while the fiber mesh F1.3 exhibited small degradation after $\sim 2 \times 10^4$ cycles (see animation in Online Resources 1 and 2). The composite film CF1. A showed no signs of degradation after $\sim 2 \times 10^4$ cycles.

Altogether, the coating of the fiber meshes resulted in phosphorescent materials with favorable mechanical properties such as high flexibility and strength. This renders them ideal candidates for applications where mobility and robustness of the indicator is crucial.

### 3.7. Oxygen mapping using a smartphone camera

The use of a smartphone camera for oxygen concentration measurements was demonstrated (see film CF1 in Fig. 5(a–d) (see also section S13, Supplementary Material). In detail, we used films CF1, F1.3 and D1, and a digital phone (Redmi 9, Xiaomi) camera, which were placed in an enclosure with controlled oxygen concentration (V/V). Notably, high performance films described elsewhere (Salaris et al., 2022) lacked the flexibility to conform onto the curved surface chosen here.

The same oxygen concentrations were tested as in section 3.4 and the oxygen maps produced were based on the light intensity values of the red channel of the RGB data from the camera. Despite the lack of an optical filter and amplification circuitry, the camera produced a more linear Stern-Volmer plot (half-sensitivity point of 29% versus 17% V/V) with higher maximum sensitivity values (9.6 versus 8.5), when comparing the PD to the best 50 performing pixels. This is a significant result as it could lead to high performance, cost-efficient oxygen sensors. Moreover, the film was placed on top of a 3 mm hole from where varying levels of nitrogen flow were used (0.1–0.4 l/min). This resulted in oxygen gradients within the film, captured with the red channel of the camera (Fig. 5 e–h). Overall, these results clearly demonstrate the capability of 2D measurements on curved surfaces and the potential for amelioration of the oxygen sensing performance of similar devices when using a smartphone camera.

It should be noted that humidity, LED intensity, photostability and temperature effects were further investigated and are included in the Supplementary Material (sections S14, S15, S16 and S17, respectively).

## 4. Conclusions

In this study, the oxygen sensitive dye PtOEP was encapsulated in nonwoven fiber meshes using solution blowing with the purpose of cell culture and human health monitoring. Specifically, two different solvents (THF and DMF) and four different polymers (PS, Ecoflex, EC and TPU) were used to fabricate fibrous films with varying mechanical and morphological properties. The experimental procedure included composition, morphology, tensile strength, oxygen sensing, and biocompatibility characterizations. Dip coating of the fiber meshes with silicone rubbers was performed for increased robustness. The coated fiber meshes were characterized in terms of their mechanical and oxygen sensing properties and the effect of humidity was investigated. Also, oxygen maps were produced using a smartphone camera and basic colorimetry techniques.

The main findings include: i) the fiber meshes were a combination of the polymers in the solutions in terms of their chemical composition; ii) the composition of the solution determined the average fiber diameter; iii) similar mechanical properties were observed for all fibers, and the highest Young's modulus was achieved with the PS and Ecoflex composite; iv) improved oxygen sensing properties were reported; v) no cytotoxicity was observed; vi) robust mechanical properties were achieved by coating the fiber meshes with silicone rubbers and vi) oxygen sensing maps were demonstrated with the use of a smartphone camera.

To summarize, the implementation of solution blowing led to phosphorescent fiber meshes with a controllable range of morphological characteristics and favorable mechanical and oxygen sensing properties. Importantly, the materials and fabrication method employed here consist of a low-cost solution of achieving phosphorescent films with improved characteristics. Thus, this allows for the wide scale availability of sensors with high mechanical strength and flexibility. Potential applications include the monitoring of tissue oxygenation with wearable medical devices and oxygen mapping of bioengineered organs in cell cultures. For example, the high surface-area-to-volume ratio and high porosity of fibrous mats have shown great promise for wound dressing and by extension wound healing monitoring (Abrigo et al., 2014). In addition, this would be especially beneficial for cases where high contact area, surface conformity and mechanical robustness are crucial.

In terms of further studies, it is suggested that a link between the wetting of the fibers and the resulting mechanical properties of the composites is investigated. This may also help ascertain the optimal coating thickness, which in turn would allow for conformal skin contact (pertinent in wearable applications) and lower response/recovery times. Also, an in-depth characterization of the fabrication parameters that affected fiber diameter and fiber alignment in the resulting meshes should be investigated. This will potentially enable further enhancement of the mechanical and sensing properties.

## CRediT authorship contribution statement

**Nikolaos Salaris:** Writing – review & editing, Writing – original draft, Visualization, Validation, Supervision, Software, Methodology, Investigation, Formal analysis, Data curation, Conceptualization.

**Wenqing Chen:** Writing – original draft, Methodology, Investigation, Formal analysis, Data curation. **Paul Haigh:** Writing – review & editing, Supervision, Conceptualization. **Lorenzo Caciolli:** Writing – review & editing, Data curation. **Giovanni Giuseppe Giobbe:** Writing – review & editing, Data curation. **Paolo De Coppi:** Supervision, Resources, Project administration, Funding acquisition. **Ioannis Papakonstantinou:** Supervision, Resources, Project administration, Conceptualization. **Manish K. Tiwari:** Writing – review & editing, Writing – original draft, Visualization, Supervision, Resources, Project administration, Funding acquisition, Formal analysis, Conceptualization.

## Declaration of competing interest

The authors declare that they have no known competing financial interests or personal relationships that could have appeared to influence the work reported in this paper.

## Data availability

Data will be made available on request.

## Acknowledgments

This work is partially supported by the Wellcome/EPSRC Centre for Interventional and Surgical Sciences (WEISS) (203145Z/16/Z), the NICEDROPS project supported by the European Research Council (ERC) under the European Union's Horizon 2020 research and innovation programme under grant agreement no. 714712 and EPSRC CDT Studentship for NS. This research was supported by the NIHR GOSH BRC. The views expressed are those of the author(s) and not necessarily those of the NHS, the NIHR or the Department of Health. MKT also acknowledges the Royal Society Wolfson Fellowship.

## Appendix A. Supplementary data

Supplementary data to this article can be found online at https://doi.org/10.1016/j.bios.2024.116198.

## References

Abrigo, M., McArthur, S.L., Kingshott, P., 2014. Electrospun nanofibers as dressings for chronic wound care: advances, challenges, and future prospects. Macromol. Biosci. 14 (6), 772–792. https://doi.org/10.1002/mabi.201300561. Wiley-VCH Verlag.

Agarwal, S., Wendorff, J.H., Greiner, A., 2008. Use of electrospinning technique for biomedical applications. Polymer (Guildf) 49 (26), 5603–5621.

Ahn, C.B., Son, K.H., Yu, Y.S., Kim, T.H., Lee, J.I., Lee, J.W., 2019. Development of a flexible 3D printed scaffold with a cell-adhesive surface for artificial trachea. Biomed. Mater. 14 (5), 55001.

Altman, G.H., et al., 2002. Cell differentiation by mechanical stress. Faseb. J. 16 (2), 1–13.

Amao, Y., 2003. Probes and polymers for optical sensing of oxygen. Microchim. Acta 143 (1), 1–12.

Baker, S.C., et al., 2006. Characterisation of electrospun polystyrene scaffolds for three-dimensional in vitro biological studies. Biomaterials 27 (16), 3136–3146.

Behrens, A.M., et al., 2014a. In situ deposition of PLGA nanofibers via solution blow spinning. ACS Macro Lett. 3 (3), 249–254.

Behrens, A.M., et al., 2014b. In situ deposition of PLGA nanofibers via solution blow spinning. ACS Macro Lett. 3 (3), 249–254. https://doi.org/10.1021/mz500049x. Mar.

Bishop, A., 2013, 9. Role of Oxygen in Wound Healing, vol. 17, pp. 399–402. https://doi.org/10.12968/JOWC.2008.17.9.30937. Sep.

Biswas, S., Shao, Y., Hachisu, T., Nguyen-Dang, T., Visell, Y., 2020. Integrated soft optoelectronics for wearable health monitoring. Adv Mater Technol 5 (8), 2000347.

Bui, V.-T., Choi, J.S., Choi, H.-S., 2018. Ordered cylindrical micropatterned Petri dishes used as scaffolds for cell growth. others J. Colloid Interface Sci. 513, 161–169.

Caicedo-Carvajal, C.E., Liu, Q., Remache, Y., Goy, A., Suh, K.S., 2011. Cancer tissue engineering: a novel 3D polystyrene scaffold for in vitro isolation and amplification of lymphoma cancer cells from heterogeneous cell mixtures. J. Tissue Eng. 2011.

Carraway, Elizabeth R., et al., 1991. Photophysics and photochemistry of oxygen sensors based on luminescent transition-metal complexes. Anal. Chem. 63 (4), 337–342.

da Silva, M.L., et al., 2010. Cartilage tissue engineering using electrospun PCL nanofiber meshes and MSCs. Biomacromolecules 11 (12), 3228–3236.

Dadol, G.C., et al., 2020. Solution blow spinning (SBS) and SBS-spun nanofibers: materials, methods, and applications. Mater. Today Commun. 25, 101656.

Daristotle, J.L., Behrens, A.M., Sandler, A.D., Kofinas, P., 2016. A review of the fundamental principles and applications of solution blow spinning. ACS Appl. Mater. Interfaces 8 (51), 34951–34963.

Favre, E., Schaetzel, P., Nguygen, Q.T., Clement, R., Neel, J., 1994. Sorption, diffusion and vapor permeation of various penetrants through dense poly (dimethylsiloxane) membranes: a transport analysis. J. Membr. Sci. 92 (2), 169–184.

Gao, Y., et al., 2021. Recent progress and challenges in solution blow spinning. Mater. Horiz. 8 (2), 426–446.

Garvin, J., Qi, J., Maloney, M., Banes, A.J., 2003. Novel system for engineering bioartificial tendons and application of mechanical load. Tissue Eng. 9 (5), 967–979.

Gerecht, S., Burdick, J.A., Ferreira, L.S., Townsend, S.A., Langer, R., Vunjak-Novakovic, G., 2007. Hyaluronic acid hydrogel for controlled self-renewal and differentiation of human embryonic stem cells. Proc. Natl. Acad. Sci. USA 104 (27), 11298–11303.

Gerecht-Nir, S., Cohen, S., Ziskind, A., Itskovitz-Eldor, J., 2004. Three-dimensional porous alginate scaffolds provide a conducive environment for generation of well-vascularized embryoid bodies from human embryonic stem cells. Biotechnol. Bioeng. 88 (3), 313–320.

Grist, S.M., Chrostowski, L., Cheung, K.C., 2010. Optical oxygen sensors for applications in microfluidic cell culture. Sensors 10 (10), 9286–9316.

Guo, X., Huang, Y., Cai, X., Liu, C., Liu, P., 2016. Capacitive wearable tactile sensor based on smart textile substrate with carbon black/silicone rubber composite dielectric. Meas. Sci. Technol. 27 (4), 45105.

Hong, S., Kim, G., 2010. Electrospun micro/nanofibrous conduits composed of poly(ε-caprolactone) and small intestine submucosa powder for nerve tissue regeneration. J. Biomed. Mater. Res. B Appl. Biomater. 94 (2), 421–428. https://doi.org/10.1002/jbm.b.31670.

Huang, C., Kamra, T., Chaudhary, S., Shen, X., 2014. Breath figure patterns made easy. ACS Appl. Mater. Interfaces 6 (8), 5971–5976.

Jenie, S.N.A., Plush, S.E., Voelcker, N.H., 2017. Singlet oxygen detection on a nanostructured porous silicon thin film via photonic luminescence enhancements. Langmuir 33 (35), 8606–8613.

Jun, I., Han, H.-S., Edwards, J.R., Jeon, H., 2018. Electrospun fibrous scaffolds for tissue engineering: viewpoints on architecture and fabrication. Int. J. Mol. Sci. 19 (3), 745.

Kumar, P., Vasita, R., 2017. Understanding the relation between structural and mechanical properties of electrospun fiber mesh through uniaxial tensile testing. J. Appl. Polym. Sci. 134 (26).

Lee, S., Park, J.-W., 2017. Luminescent oxygen sensors with highly improved sensitivity based on a porous sensing film with increased oxygen accessibility and photoluminescence. Sensor. Actuator. B Chem. 249, 364–377.

Lee, J.-H., Kwon, J.-S., Kim, Y.-H., Choi, E.-H., Kim, K.-M., Kim, K.-N., 2013. The effects of enhancing the surface energy of a polystyrene plate by air atmospheric pressure plasma jet on early attachment of fibroblast under moving incubation. Thin Solid Films 547, 99–105.

Leong, M.F., Lu, H.F., Lim, T.C., Du, C., Ma, N.K.L., Wan, A.C.A., 2016. Electrospun polystyrene scaffolds as a synthetic substrate for xeno-free expansion and differentiation of human induced pluripotent stem cells. Acta Biomater. 46, 266–277.

Lerman, M.J., Lembong, J., Muramoto, S., Gillen, G., Fisher, J.P., 2018. The evolution of polystyrene as a cell culture material. Tissue Eng., Part B 24 (5), 359–372.

Li, Z., et al., 2014. Non-invasive transdermal two-dimensional mapping of cutaneous oxygenation with a rapid-drying liquid bandage. Biomed. Opt Express 5 (11), 3748. https://doi.org/10.1364/boe.5.003748. Nov.

Li, Xiaolei, et al., 2021. Optimization of bright, highly flexible, and humidity insensitive porphyrin-based oxygen-sensing materials. J. Mater. Chem. C 9 (24), 7555–7567.

Lim, H.-R., Kim, H.S., Qazi, R., Kwon, Y.-T., Jeong, J.-W., Yeo, W.-H., 2020. Advanced soft materials, sensor integrations, and applications of wearable flexible hybrid electronics in healthcare, energy, and environment. Adv. Mater. 32 (15), 1901924.

Liu, R., et al., 2011. Microporous phase-separated films of polymer blends for enhanced outcoupling of light from OLEDs. Opt Express 19 (106), A1272–A1280.

Liu, R., Xiao, T., Cui, W., Shinar, J., Shinar, R., 2013. Multiple approaches for enhancing all-organic electronics photoluminescent sensors: simultaneous oxygen and pH monitoring. Anal. Chim. Acta 778, 70–78.

Majumder, S., Mondal, T., Deen, M.J., 2017. Wearable sensors for remote health monitoring. Sensors 17 (1), 130.

Mao, Y., et al., 2017. Highly enhanced sensitivity of optical oxygen sensors using microstructured PtTFPP/PDMS-pillar arrays sensing layer. Sensor. Actuator. B Chem. 251, 495–502.

McDonagh, C., MacCraith, B.D., McEvoy, A.K., 1998. Tailoring of sol- gel films for optical sensing of oxygen in gas and aqueous phase. Anal. Chem. 70 (1), 45–50.

McEvoy, A.K., McDonagh, C.M., MacCraith, B.D., 1996. Dissolved oxygen sensor based on fluorescence quenching of oxygen-sensitive ruthenium complexes immobilized in sol–gel-derived porous silica coatings. Analyst 121 (6), 785–788.

Mikulchyk, T., Martin, S., Naydenova, I., 2013. Humidity and temperature effect on properties of transmission gratings recorded in PVA/AA-based photopolymer layers. J. Opt. 15 (10), 105301.

Mostafalu, P., Lenk, W., Dokmeci, M.R., Ziaie, B., Khademhosseini, A., Sonkusale, S.R., 2015. Wireless flexible smart bandage for continuous monitoring of wound oxygenation. IEEE Trans Biomed. Circuits Syst. 9 (5), 670–677. https://doi.org/10.1109/TBCAS.2015.2488582. Oct.

Nam, J., Johnson, J., Lannutti, J.J., Agarwal, S., 2011. Modulation of embryonic mesenchymal progenitor cell differentiation via control over pure mechanical modulus in electrospun nanofibers. Acta Biomater. 7 (4), 1516–1524. https://doi.org/10.1016/j.actbio.2010.11.022.

Ochoa, M., et al., 2020. Integrated sensing and delivery of oxygen for next-generation smart wound dressings. Microsyst. Nanoeng. 6 (1) https://doi.org/10.1038/s41378-020-0141-7. Dec.

Papkovsky, D.B., Dmitriev, R.I., 2013. Biological detection by optical oxygen sensing. Chem. Soc. Rev. 42 (22), 8700–8732.

Paraboschi, I., De Coppi, P., Stoyanov, D., Anderson, J., Giuliani, S., 2021. Fluorescence imaging in pediatric surgery: state-of-the-art and future perspectives. W.B. Saunders J. Pediatr. Surg. 56 (4), 655–662. https://doi.org/10.1016/j.jpedsurg.2020.08.004. Apr. 01.

Polat, Y., et al., 2016. Solution blowing of thermoplastic polyurethane nanofibers: a facile method to produce flexible porous materials. J. Appl. Polym. Sci. 133 (9).

Prabhakaran, M.P., et al., 2008. Electrospun biocomposite nanofibrous scaffolds for neural tissue engineering. Tissue Eng Part A 14 (11), 1787–1797.

Presley, K., Shahhosseini, M., Shi, D., Castro, C., Lannutti, J., 2019. Analysis of long-term optical performance of phosphorescent oxygen sensing polymeric nanofibers. Polym. Test. 80 https://doi.org/10.1016/j.polymertesting.2019.106127. Dec.

Ratner, B.D., Hoffman, A.S., Schoen, F.J., Lemons, J.E., 2004. Biomaterials Science: an Introduction to Materials in Medicine. Elsevier.

Sabbatier, G., Abadie, P., Dieval, F., Durand, B., Laroche, G., 2014. Evaluation of an air spinning process to produce tailored biosynthetic nanofibre scaffolds. Mater. Sci. Eng. C 35, 347–353.

Salaris, N., Haigh, P., Papakonstantinou, I., Tiwari, M.K., 2022. Self-assembled porous polymer films for improved oxygen sensing. Sensor. Actuator. B Chem., 132794

Sen, C.K., 2009. Wound healing essentials: let there be oxygen. Wound Repair Regen. 17 (1), 1–18. https://doi.org/10.1111/j.1524-475X.2008.00436.x. Jan.

Shi, H., et al., 2014. Ultrasmall phosphorescent polymer dots for ratiometric oxygen sensing and photodynamic cancer therapy. Adv. Funct. Mater. 24 (30), 4823–4830.

Sinha-Ray, S., Zhang, Y., Yarin, A.L., Davis, S.C., Pourdeyhimi, B., 2011. Solution blowing of soy protein fibers. Biomacromolecules 12 (6), 2357–2363.

Srinivasan, S., Chhatre, S.S., Mabry, J.M., Cohen, R.E., McKinley, G.H., 2011. Solution spraying of poly (methyl methacrylate) blends to fabricate microtextured, superoleophobic surfaces. Polymer (Guildf) 52 (14), 3209–3218.

Stone, H.B., Brown, J.M., Phillips, T.L., Sutherland, R.M., 1993. Oxygen in human tumors: correlations between methods of measurement and response to therapy: summary of a workshop held November 19-20, 1992, at the National Cancer Institute, Bethesda, Maryland. Radiat. Res. 136 (3), 422–434.

Sun, T., Mai, S., Norton, D., Haycock, J.W., Ryan, A.J., Macneil, S., 2005. Self-organization of skin cells in three-dimensional electrospun polystyrene scaffolds. Tissue Eng. 11 (7–8), 1023–1033.

Tavakol, D.N., et al., 2020. Oxygen-sensing biomaterial construct for clinical monitoring of wound healing. Adv. Skin Wound Care 33 (8), 428–436. https://doi.org/10.1097/01.ASW.0000666912.86854.2b. Aug.

Tayfun, U., Kanbur, Y., Abac, U., Güney, H.Y., Bayraml, E., 2017. Mechanical, electrical, and melt flow properties of polyurethane elastomer/surface-modified carbon nanotube composites. J. Compos. Mater. 51 (14), 1987–1996.

Tutak, W., et al., 2013. The support of bone marrow stromal cell differentiation by airbrushed nanofiber scaffolds. Biomaterials 34 (10), 2389–2398.

Vunjak-Novakovic, G., Altman, G., Horan, R., Kaplan, D.L., 2004. Tissue engineering of ligaments. Annu. Rev. Biomed. Eng. 6, 131–156.

Wang, F., Yao, Q., 2023. Oxygen sensing performance improvement by the combination of narrowed electrospinning fibers and multi-cored phosphorescent photosensitizer: strategy and performance comparison. J. Mol. Struct. 1275 (Mar) https://doi.org/10.1016/j.molstruc.2022.134592.

Wang, N., et al., 2001. Mechanical behavior in living cells consistent with the tensegrity model. Proc. Natl. Acad. Sci. USA 98 (14), 7765–7770.

Wang, Y., et al., 2011. High-performance oxygen sensors based on EuIII complex/polystyrene composite nanofibrous membranes prepared by electrospinning. ChemPhysChem 12 (2), 349–355. https://doi.org/10.1002/cphc.201000884. Feb.

Webb, R.C., et al., 2015. Materials Science/Clinical Medi Cine: epidermal devices for noninvasive, precise, and continuous mapping of macrovascular and microvascular blood flow. Sci. Adv. 1 (9) https://doi.org/10.1126/sciadv.1500701. Oct.

Wu, X., Suvarnapathaki, S., Walsh, K., Camci-Unal, G., 2018. Paper as a scaffold for cell cultures: teaching an old material new tricks. MRS Commun. 8 (1), 1–14.

Xue, R., Behera, P., Xu, J., Viapiano, M.S., Lannutti, J.J., 2014. Polydimethylsiloxane core–polycaprolactone shell nanofibers as biocompatible, real-time oxygen sensors. Sensor. Actuator. B Chem. 192, 697–707.

Zhang, L., Kopperstad, P., West, M., Hedin, N., Fong, H., 2009. Generation of polymer ultrafine fibers through solution (air-) blowing. J. Appl. Polym. Sci. 114 (6), 3479–3486.

Zhang, J., Kitayama, H., Gotoh, Y., 2020. High strength ultrafine cellulose fibers generated by solution blow spinning. Eur. Polym. J. 125, 109513 https://doi.org/10.1016/J.EURPOLYMJ.2020.109513. Feb.